

Non-linearity and temporal changes of fault zone site response associated with strong ground motion

Chunquan Wu,¹ Zhigang Peng¹ and Yehuda Ben-Zion²

¹*School of Earth and Atmospheric Sciences, Georgia Institute of Technology, Atlanta, GA, 30332, USA. E-mail: chunquanwu@gatech.edu*

²*Department of Earth Sciences, University of Southern California, Los Angeles, CA 90089-0740, USA*

Accepted 2008 October 5. Received 2008 August 7; in original form 2008 April 13

SUMMARY

We systematically analyse temporal changes of fault zone (FZ) site response along the Karadere-Düzce branch of the North Anatolian fault that ruptured during the 1999 İzmit and Düzce earthquake sequences. The study is based primarily on spectral ratios of strong motion seismic data recorded by a FZ station and a station ~400 m away from the fault and augmented by analysis of weak motion records. The observations are used to track non-linear behaviour and temporal changes of the FZ site response. The peak spectral ratio increases 80–150 per cent and the peak frequency drops 20–40 per cent at the time of the Düzce main shock. These co-main shock changes are followed by a logarithmic recovery over an apparent timescale of ~1 d. However, analysis of temporal changes at each individual station using weak motion waveforms generated by repeating earthquakes show lower-amplitude longer-duration logarithmic recoveries that are not detected by the spectral ratio analysis. The results are consistent with a reduction of *S*-wave velocities in the top 100–300 m during the Düzce main shock of 20–50 per cent or more and logarithmic post-main shock recovery on a timescale of 3 months or more. The observations support previous suggestions that non-linear wave propagation effects and temporal changes of seismic properties are generated in the shallow material by strong ground motion of nearby major earthquakes.

Key words: Elasticity and anelasticity; Fault zone rheology; Earthquake ground motions; Site effects; Wave propagation.

1 INTRODUCTION

Large earthquakes occur on major fault zone (FZ) structures. The faulting process produces localized belts of damaged FZ rocks that have lower elastic moduli than the surrounding rocks (e.g. Ben-Zion & Sammis 2003, and references therein). The FZ damage is pronounced in the top few kilometres of the crust, because increasing normal stress suppresses the damage generation and enhances the healing process of damage recovery (e.g. Lyakhovskiy *et al.* 1997; Ben-Zion & Shi 2005; Johnson & Jia 2005; Rice *et al.* 2005; Finzi *et al.* 2008). The top few hundred metres of the crust away from faults are also heavily fractured due to weathering processes, seismic motions, seasonal thermoelastic strain and other forces that operate under very low normal stress conditions. The shallow surface layers are characterized by extremely low shear wave velocity (~200–400 m s⁻¹) and very high attenuation ($Q \sim 1-10$; e.g. Aster & Shearer 1991). Quantifying the temporal changes of material properties within and around active FZs and in the near-surface layers is important for better understanding rock rheology and estimating the strong ground motion that can be generated by large earthquakes.

As high-amplitude seismic waves propagate through damaged FZ rocks and/or shallow surface layers, they may produce additional damage leading to non-linear wave propagation effects and temporal changes of material properties (e.g. seismic velocity, attenuation). Recent studies based on waveform cross-correlations of repeating earthquakes showed clear changes of seismic velocities in shallow surface layers and around active FZs, with rapid reductions during strong motions of nearby large earthquakes followed by logarithmic recoveries (e.g. Rubinstein & Beroza 2004a, b, 2005; Peng & Ben-Zion 2006; Rubinstein *et al.* 2007). The use of repeating earthquakes allows separation of spatial variations from temporal changes of material properties (e.g. Peng & Ben-Zion 2005, 2006) but is limited by the availability of repeating earthquakes in the study area. Some studies employed repeating artificial sources (e.g. Li *et al.* 1998, 2006; Vidale & Li 2003), but these types of studies are limited by high cost and poor depth penetration.

Another technique that has been widely applied to study non-linear site response of surface layers and sediments is the spectral ratio method (e.g. Beresnev & Wen 1996; Field *et al.* 1997; Pavlenko & Irikura 2003; Sawazaki *et al.* 2006, 2008). This method generally involves comparisons of weak and strong-motion responses based

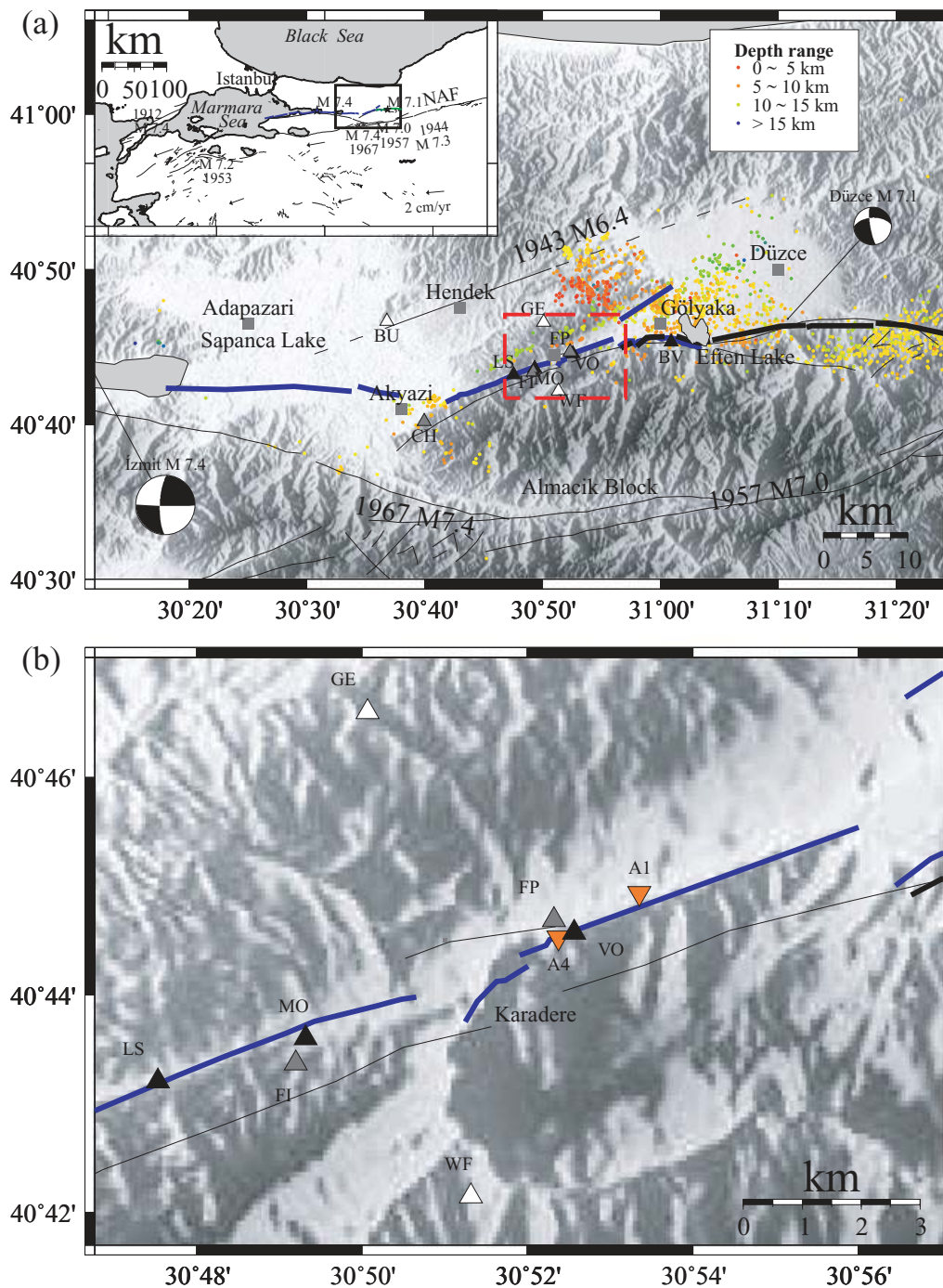


Figure 1. (a) Topographic map of the area along the Karadere-Düzce branch of the North Anatolian fault (NAF). Earthquake locations are marked by small dots with colours denoting different depth ranges. Shaded background indicates topography with white being low and dark being high. The surface ruptures of the İzmit and Düzce earthquakes are indicated with blue and black lines, respectively. Dark thin lines associated with earthquake information denote faults that were active during recent ruptures. Other dark thin lines are geologically inferred fault traces. Stations within, near and outside the FZ are shaded with dark, grey and white triangles, respectively. Grey squares denote locations of nearby cities. The area bounded by the red dashed lines is shown in (b). The inset illustrates the tectonic environment in northwestern Turkey with the box corresponding to our study area. Vectors represent plate deformation rate (Reilinger *et al.* 1997) from GPS data. Modified from Peng & Ben-Zion (2006). (b) A zoom-in map around the location of the station VO inside the fault and FP ~400 m away from the fault. All the symbols and notations are the same as in (a). The inverted triangles mark seismic stations A1 and A4 used in the study of Karabulut & Bouchon (2007).

on the spectral ratio between a target and a reference site (e.g. nearby hard rock site or borehole). Recently, Karabulut & Bouchon (2007) applied the spectral ratio method to near-fault ground accelerations to quantify spatial variability and non-linearity along the Karadere-

Düzce branch of the North Anatolian fault (NAF) in relation to the 1999 M_w 7.1 Düzce earthquake (Fig. 1). Their results indicated ~45 per cent reduction in S -wave velocity during the Düzce main shock and near-instantaneous recovery. In comparison, based on

waveform cross-correlations of weak motion generated by repeating earthquakes in the same region, Peng & Ben-Zion (2006) found a much smaller percentage of coseismic reduction in *S*-wave velocity (up to 3 per cent) and a much longer timescale of recovery (at least 3 months). The differences may stem from different resolutions of the employed data and analysis techniques, along with different site conditions where the instruments are placed.

To better quantify temporal changes of FZ properties and investigate the differences in the above two studies, we apply the spectral ratio method to strong and weak motion data recorded by a pair of on- and off-fault stations before and during the $M_w 7.1$ Düzce earthquake and its aftershocks. The analysis of the strong ground motion shows a 20–40 per cent reduction of peak frequency (frequency of maximum spectral ratio amplitude) and 80–150 per cent increase of peak spectral ratios (maximum of spectral ratio amplitude) at the FZ station immediately following the Düzce main shock, consistent with the ~45 per cent reduction in *S*-wave velocity found by Karabulut & Bouchon (2007). These strong changes of spectral ratios are followed by a logarithmic recovery to the values before the main shock within ~1 d. The on-scale weak motion data used in the spectral ratio analysis start only ~6 hr after the Düzce main shock and show mild evolution of peak spectral frequency afterwards (within large error bars), consistent generally with the results of Peng & Ben-Zion (2006). In the following Sections 2 and 3, we describe the seismic data, analysis procedure and results. In Section 4, we present synthetic waveform simulations for sets of varying FZ properties that can explain the observed changes. We compare our results with those from previous studies in Section 5, and discuss possible mechanisms that might be responsible for the observations in Section 6.

2 DATA AND ANALYSIS PROCEDURE

2.1 Seismic data

The analysis employs primarily strong and weak motion data recorded by two stations VO and FP from a temporary 10-station PASSCAL seismic network (Fig. 1a) along and around the Karadere-Düzce branch of NAF that was deployed a week after the 1999 August 17 $M_w 7.4$ İzmit earthquake (Seeber *et al.* 2000; Ben-Zion *et al.* 2003). All 10 stations had REFTEK recorders and 3-component L22 short-period sensors with a sampling frequency of 100 Hz. In addition, eight stations (not including MO and GE) had 3-component force-balance accelerometers (FBAs). During the 6-month operational period, this network recorded seismograms of about 26 000 earthquakes, including the 1999 November 12 $M_w 7.1$ Düzce main shock, its foreshocks and aftershocks.

We use seismic waveforms recorded by the station pair VO and FP for the main analysis in this work because these stations form the only pair that is deployed at close distance and has both strong and weak motion recordings. In particular, station VO is deployed on a shutter ridge with high relief, composed of gouge and slope debris inside the rupture zone of the İzmit earthquake. Station FP is ~400 m off the fault in soil near bedrock with medium relief (Fig. 1b). Additional details regarding the seismic experiment and data set are given by Seeber *et al.* (2000) and Ben-Zion *et al.* (2003).

2.2 Analysis procedure

The analysis generally follows the procedures of Sawazaki *et al.* (2006) and Karabulut & Bouchon (2007) and is briefly described

here. We use the two horizontal-component ground acceleration records at stations VO and FP, which are generated by 1806 earthquakes. These include 113 events starting 8 d before the Düzce main shock, the main shock and 1692 events within 3 months after the main shock. The local magnitudes of most events range from 0 to 5, and the hypocentral depths range from 5 to 15 km. The occurrence times, magnitudes and peak ground accelerations (PGAs) associated with the employed events are shown in Fig. 2.

We analyse the entire seismic data set using two slightly different approaches. In the first approach, we use 10-s time windows with origins that are moved forward by 5 s for all waveforms recorded at stations VO and FP. In this case all possible seismic phases, including pre-event noise, *P*, *S* and coda waves are analysed together. In the second approach, we only analyse data within a 10 s long coda wave window, which starts from twice the direct *S*-wave traveltime after the origin time of each event (e.g. Sawazaki *et al.* 2006). To avoid mixing coda waves with other phases, we do not use the records in the coda-window-based analysis if there are any other events between the onset of the *S*-wave and the end of the coda window or if *S*-wave phases cannot be clearly identified.

Next, we remove the mean value of the traces and apply a 5 per cent Hanning taper to both ends. We add the power spectra of the two horizontal components and take the square root of the sum to get the amplitude of the vector sum of the two horizontal spectra. The obtained spectra are smoothed by applying the mean smoothing algorithm from the subroutine ‘smooth’ in the Seismic Analysis Code (Goldstein *et al.* 2003), with half width of five points. The spectral ratio is obtained by taking the ratio of the horizontal spectra for stations VO and FP. Fig. 3 illustrates the analysis procedure with example waveforms generated by the Düzce main shock.

The same procedure is applied to the weak motion data. We do not analyse time windows in which the peak velocity is above 80 per cent of the maximum observed level at a given station, since these windows may be associated with clipped portions of waveforms (Yang *et al.* 2007).

3 RESULTS

3.1 Strong motion data

After processing the sliding-window-based data, we obtain from the first approach 7543 spectral ratio traces, including 390 before the Düzce main shock, 7 during the main shock and 7147 after the main shock. From the coda-window-based analysis, we obtain 697 spectral ratio traces, including 54 before the main shock and 643 after the main shock. Fig. 4 shows a comparison of spectral ratios for the direct *S*-wave and the coda waves for 15 events within 2 hr after the main shock. The spectral ratios calculated from coda waves are generally similar to those calculated from the direct *S*-waves but with less scatter. This is consistent with the observations by Sawazaki *et al.* (2006) and Mayeda *et al.* (2007). This phenomenon can be attributed to the random distribution of heterogeneities and backscattered waves in the coda (Aki 1969; Aki & Chouet 1975). Such random distribution provides an averaging effect for the observed spectral ratios by making them less dependent on propagation paths than the direct *S*-wave (Phillips & Aki 1986). The disadvantage of using only the coda waves is that data in a certain time range (e.g. immediately after the main shock) may not be used due to overlapping seismic records (e.g. Peng *et al.* 2006). We therefore analyse in this study results using both approaches.

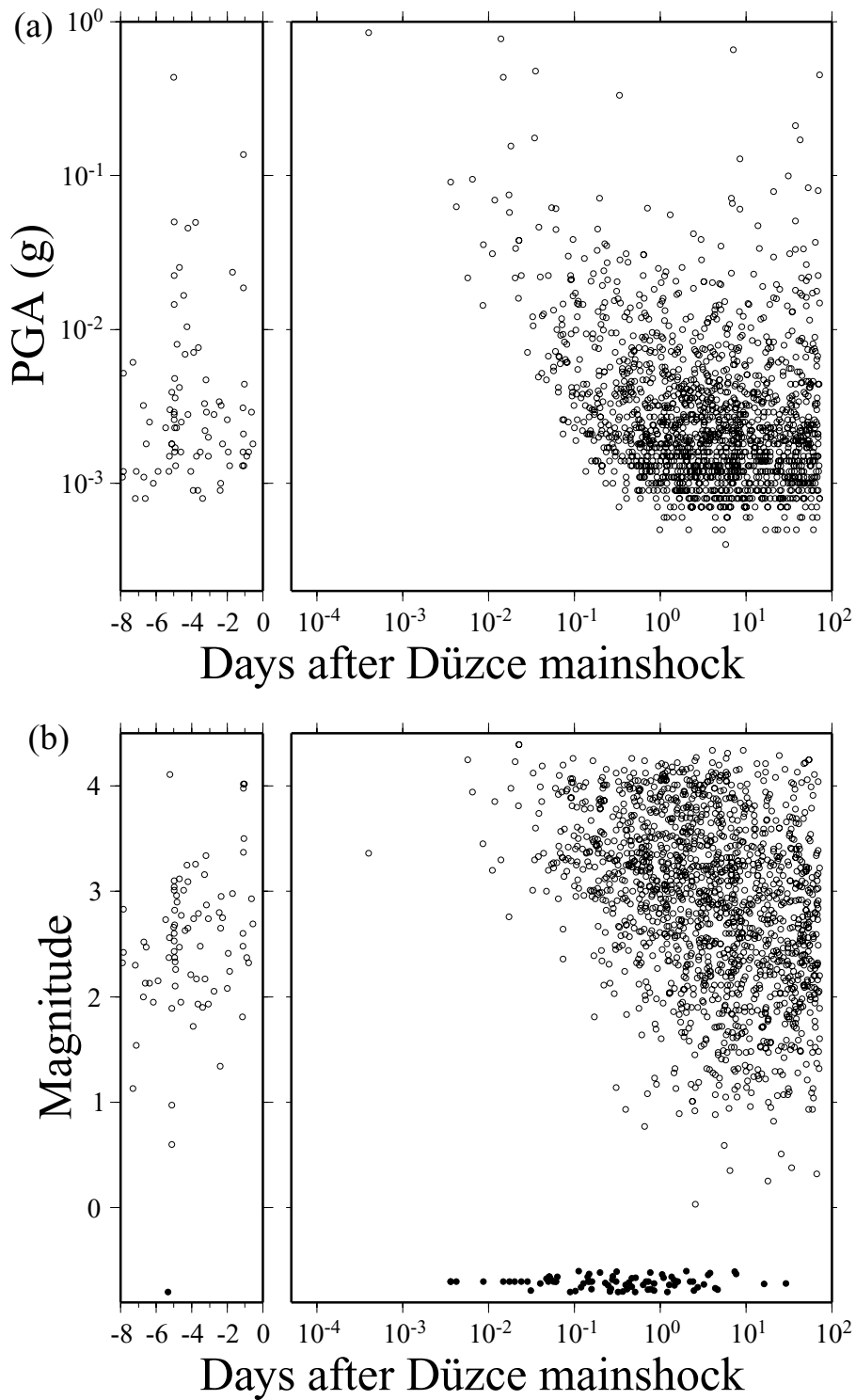


Figure 2. (a) Peak Ground Acceleration (PGA) values of the earthquakes used in this study plotted against occurrence times (days in linear scale before and logarithmic scale after the Düzce main shock). (b) Magnitudes of the earthquakes used in this study, plotted against occurrence times (same as in a). Open and filled circles mark events that have magnitudes and those that do not, respectively. The events with no magnitudes are plotted at the bottom of the figure around magnitude of -1 , with a random number added for plotting purposes.

The temporal changes of spectral ratio for all phases and coda wave windows are shown in Figs 5(a) and (b), respectively. In both plots, we observe a clear increase in peak spectral ratios and reduction in peak frequencies at the time of the main shock, followed by logarithmic recovery. To better quantify the degree of coseismic

changes and the timescale of postseismic recovery, we obtain the values of peak spectral ratios and peak frequencies for all traces and average them in different time periods. We divide the whole data set into the following periods: before the main shock, 10–30 s after the main shock, 300–1000 s after the main shock and then every

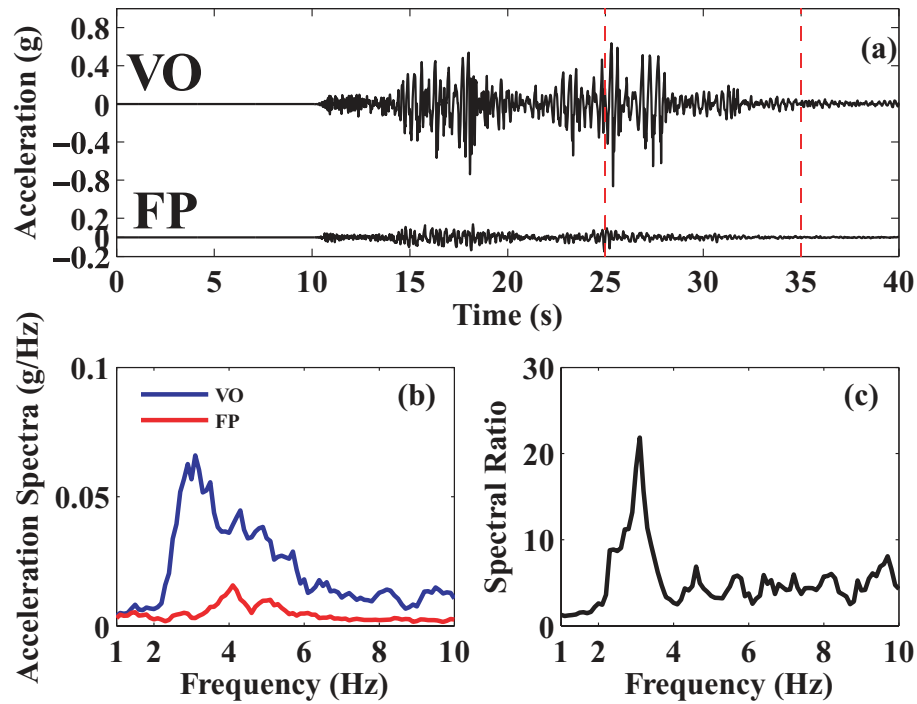


Figure 3. (a) Ground accelerations recorded at the two stations VO and FP during the 1999 *M*w 7.1 Düzce, Turkey, earthquake. The red dashed lines indicate the time window that is used to compute the spectra in (b) and spectral ratio in (c).

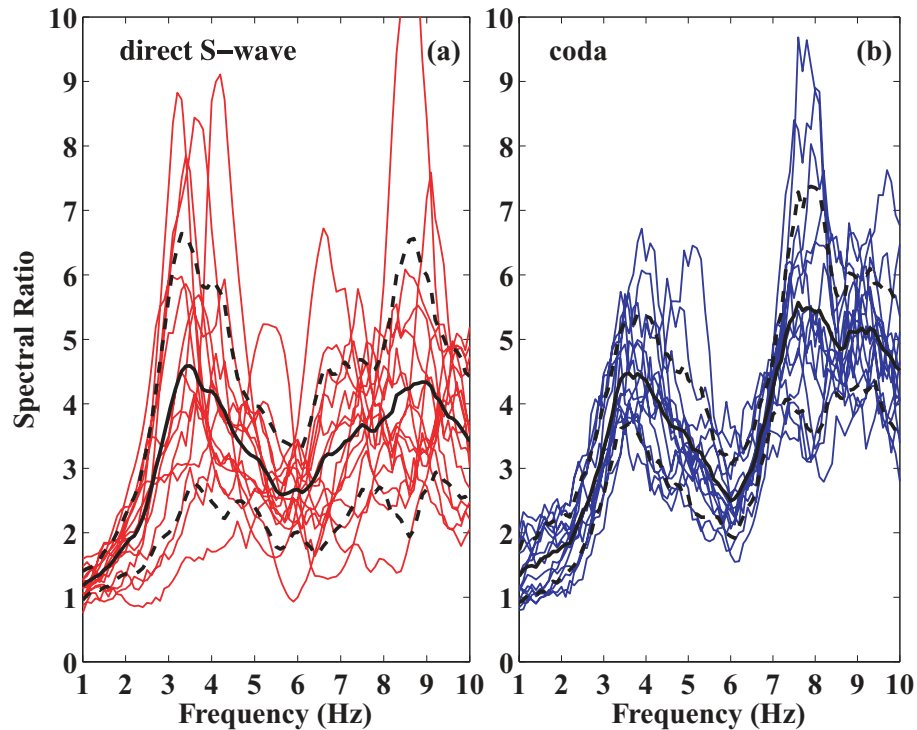


Figure 4. Spectral ratios for the strong motion data from (a) direct *S* waves and (b) coda waves for 15 events occurred within 2 hr after the Düzce main shock. The black solid and dashed lines show the average spectral ratios and the standard deviation.

0.25 interval in logarithmic timescale after 1000 s. We have tested averaging the peaks using different time windows and the obtained results remain essentially the same. We use logarithmic, instead of linear time because previous studies have found a logarithmic heal-

ing process for long-term recovery (e.g. Rubinstein & Beroza 2004; Schaff & Beroza 2004; Peng & Ben-Zion 2006; Sawazaki *et al.* 2006). Next, we compute the average of the peak spectral ratios and peak frequencies in each time period. The same procedure is

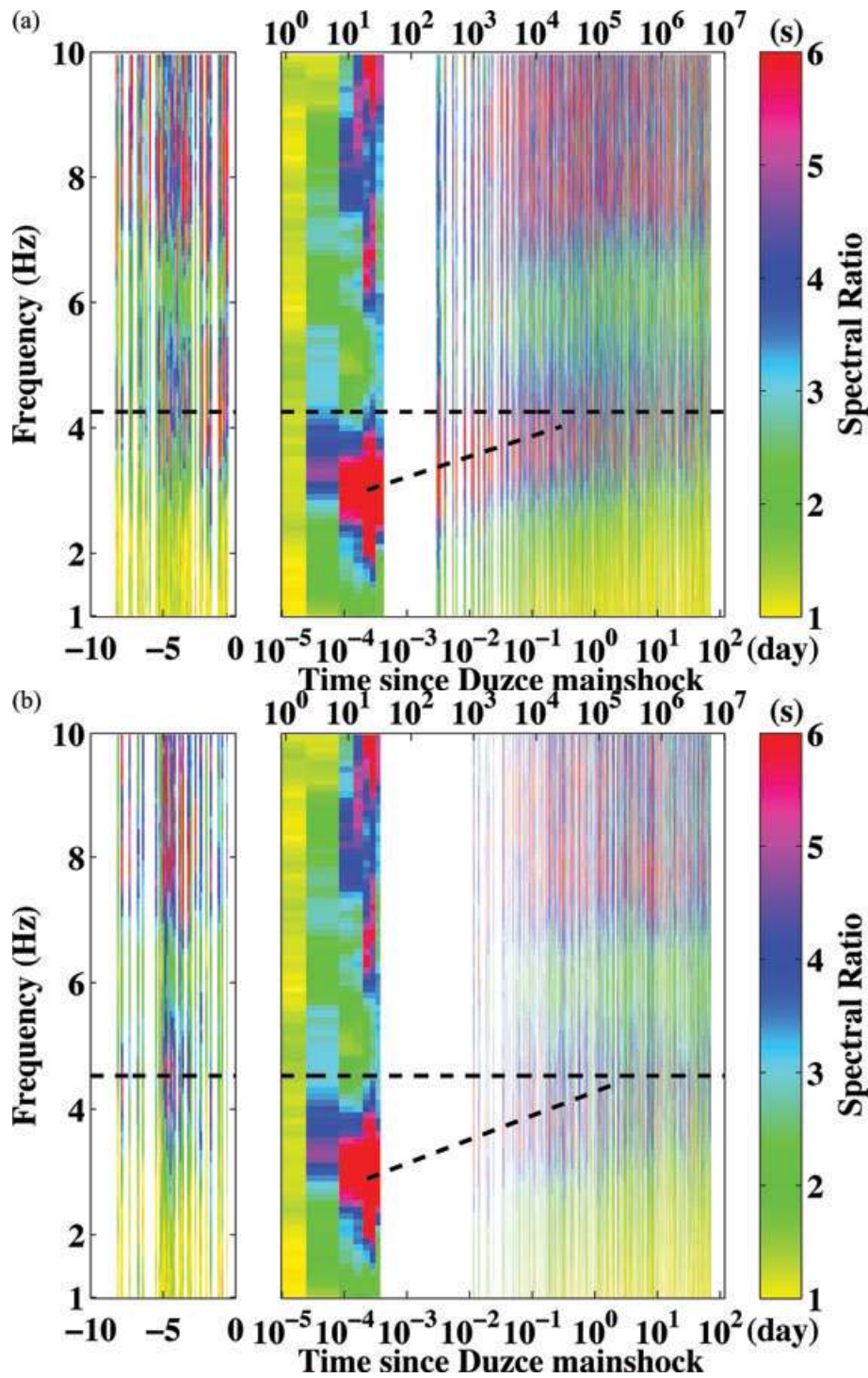


Figure 5. (a) Temporal changes of sliding-window-based spectral ratios for the strong motion data at stations VO and FP. The right bin shows the colour-coded spectral ratios for the main shock and aftershocks. The left bin shows those before the main shock. Values shown on the top and bottom of the figure indicate lapse times after the main shock in seconds and in days, respectively. White colour represents no data. The horizontal and inclined black dashed lines show the pre-main shock value and the recovery trend, respectively. (b) Temporal changes of coda-window-based spectral ratio for the strong motion data at stations VO and FP. Symbols and notations are the same as in (a).

applied to the coda-window-based spectral ratio traces. Due to lack of data and overlapping records, there are gaps in the coda-window analysis at 0–30 and 300–1000 s after the main shock.

The averaged peak spectral ratios and frequencies with their standard deviations based on the analysis with all phases and only coda

windows are shown in Figs 6(a) and (c) and 7(a) and (c), respectively. For comparison, the averaged peak spectral ratios and frequency in the period 0–30 s after the main shock from all phases are included in the results of the coda-window-based analysis (Figs 7a and c). The results from both data sets show a sudden increase of peak

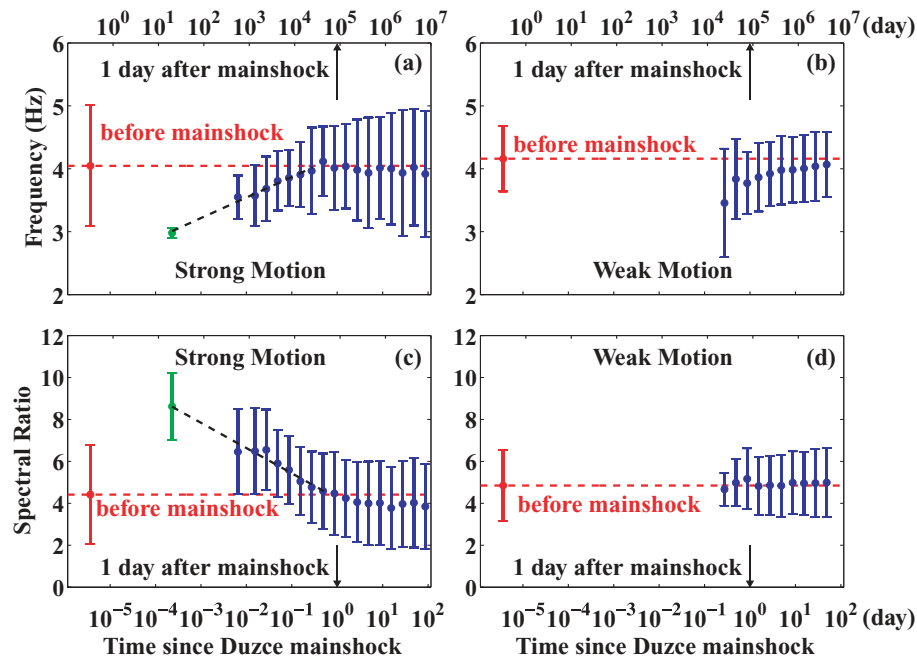


Figure 6. (a) Averaged peak frequencies from the sliding-window-based strong-motion data before (red), during (green) and after (blue) the main shock, recorded at stations VO and FP. Vertical solid bar centred at each data point shows the standard deviation. The red dashed line indicates the pre-main shock value of peak frequency. The vertical black line with arrow marks the time of 1 d after the main shock. Values shown on the top and bottom of the figure indicate lapse times after the main shock in seconds and in days, respectively. (b) Same plot as (a) for the weak motion data. (c) Averaged peak spectral ratios with the same symbols and notations as (a). (d) Same plot as (c) for the weak motion data.

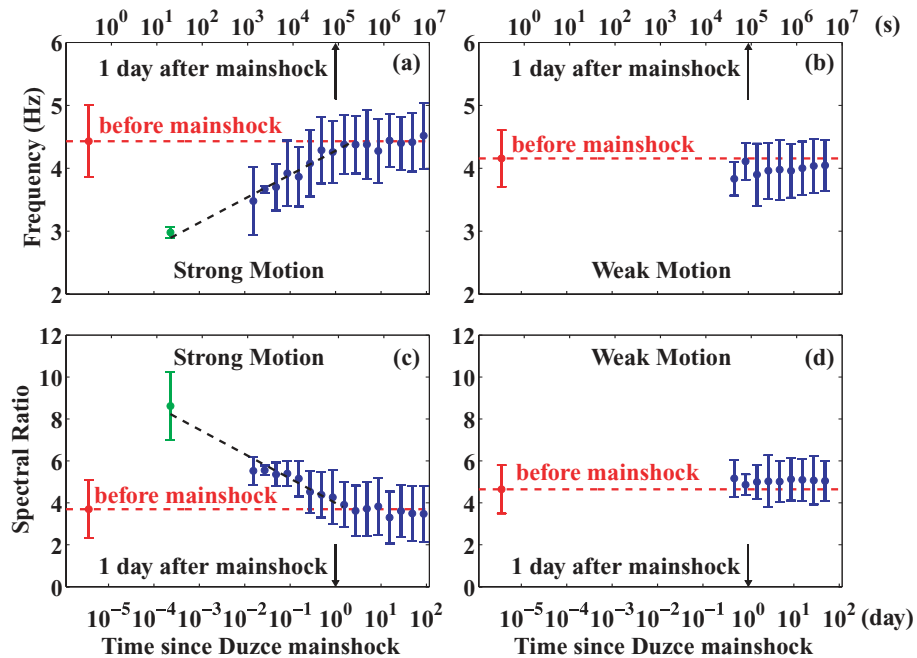


Figure 7. (a) Averaged peak frequencies from the coda-window-based strong-motion data before (red), during (green) and after (blue) the main shock, recorded at stations VO and FP. (b) Same plot as (a) for the weak motion data. (c) Averaged peak spectral ratios with the same symbols and notations as (a). (d) Same plot as (c) for the weak motion data. Other symbols and notations are the same as in Fig. 6.

spectral ratio and a shift of the spectral peak to lower frequencies during the main shock. The values of the averaged peak spectral ratios and peak frequencies, together with the increase/reduction or recovery rates before, immediately after and 1 d after the main shock are listed in Table 1. Both types of spectral ratio change show

a near-complete recovery with a timescale of ~ 1 d after the main shock.

We have performed the same analyses on the vertical component seismograms but the results did not show clear spectral peaks and temporal changes in the same frequency range. This is consistent

Table 1. Averaged peak spectral ratios, peak frequencies and increase/recovery rates with error assessments before, immediately after and 1 d after the main shock from (a) the sliding-window based analysis and (b) the coda-window based analysis.

Time period	Peak spectral ratio	Increase/Recovery rate (per cent)	Peak frequency (Hz)	Reduction/Recovery rate (per cent)
(a) The sliding-window-based analysis				
Before the main shock	4.4 (± 2.3)		4.0 (± 0.9)	
Main shock 0–30s	8.6 (± 1.6)	95 (± 31) increase	3.0 (± 0.1)	25 (± 8) reduction
One day after the main shock	4.5 (± 2.0)	98 (± 28) Recovery	4.0 (± 0.6)	100 (± 7) recovery
(b) The coda-window-based analysis				
Before the main shock	3.7 (± 1.4)		4.4 (± 0.5)	
Main shock 0–30s	8.6 (± 1.6)	132 (± 27) increase	3.0 (± 0.1)	32 (± 6) reduction
One day after the main shock	3.6 (± 1.2)	102 (± 25) recovery	4.4 (± 0.4)	100 (± 6) recovery

with observations that horizontal components are generally more sensitive to site amplification and other local structures than vertical components (e.g. Castro *et al.* 1997).

3.2 Weak motion data

Figs 6(b) and (d) and 7(b) and (d) show corresponding results for the weak motion data by applying the same averaging technique that has been used for the strong motion data. The obtained peak frequencies and spectral ratios are very similar to those from the strong motion data. Unfortunately, the results from the weak motion data lack useful data points within the first few hours after the main shock due to severe clipping of waveforms on the weak motion instruments. The peak frequencies from the time period with useful weak motion data are increasing gradually with time in the 3 months following the Düzce main shock. However, the large error bars imply that these changes are not well resolved by the employed spectral ratio technique. The amplitudes of the spectral ratios of the weak motion data do not show a clear pattern. In the following sections we focus on the results obtained from the strong motion data.

4 SYNTHESIS WAVEFORMS

In this section, we attempt to relate the observed temporal changes of peak frequency and spectral ratios to changes of elastic properties within the FZ. Assuming a low-velocity FZ layer of width W in a half-space (HS), the relation between the FZ fundamental resonance frequency f and the S -wave velocity β_{FZ} inside the FZ is given by $f = \beta_{FZ}/2W$. A shift of peak frequency to lower value during the strong ground motions of the Düzce main shock can hence be related to the coseismic reduction of the S -wave velocity inside the FZ (Karabulut & Bouchon 2007).

To quantify the relationship between the observed spectral changes and the velocity reduction in the FZ, we use the 2-D analytical solution of Ben-Zion & Aki (1990) and Ben-Zion (1998) for waveforms generated by a shear dislocation in a structure with a low-velocity FZ layer (Fig. 8). Since the velocity variations along the FZ are much smaller than those across it, the 2-D model should provide a valid simplification of the 3-D velocity variations in the vicinity of the FZ. We simulate ground motion inside and outside the FZ, using parameters obtained from analysis of FZ trapped waves in the same region (Ben-Zion *et al.* 2003). The employed parameters are: FZ width $W = 100$ m, S -wave velocities in the FZ and the

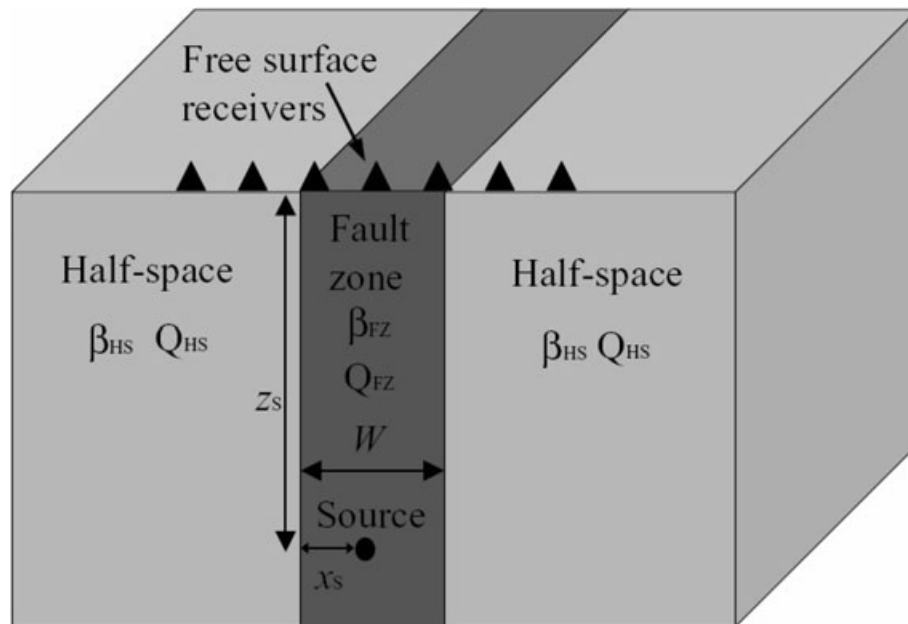


Figure 8. A three-media model for a uniform low-velocity FZ structure in a half-space. The source is an SH line dislocation with coordinates (x_S, z_S) . The width, shear attenuation coefficient and shear wave velocity of the FZ are marked by W , Q_{FZ} and β_{FZ} , respectively. The shear wave velocity and the attenuation coefficient of the HS are denoted by β_{HS} and Q_{HS} , respectively (after Ben-Zion *et al.* 2003).

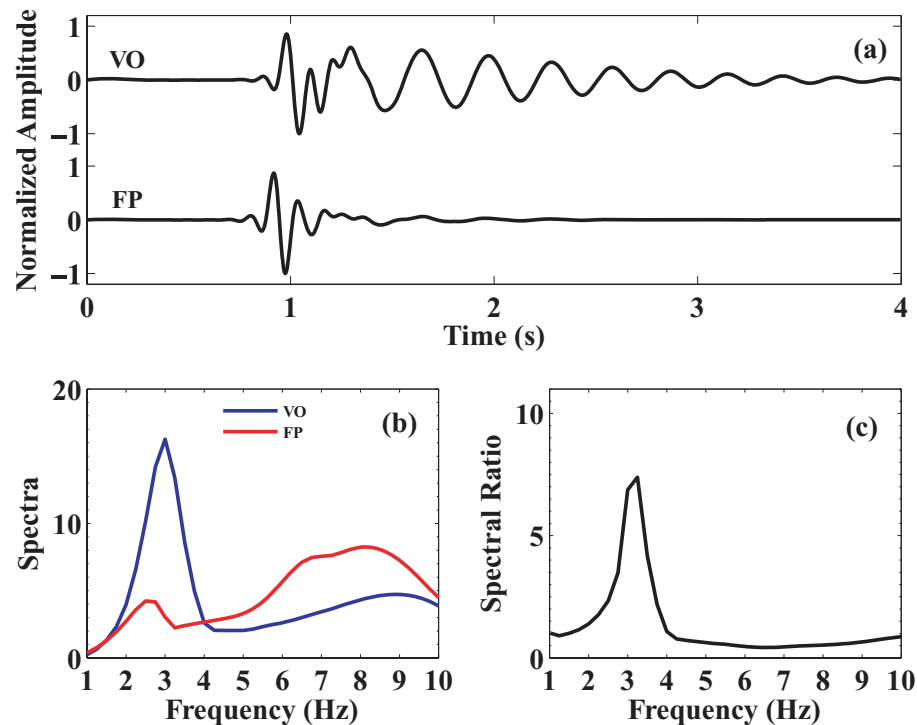


Figure 9. (a) Synthetic ground acceleration waveforms from the model in Fig. 8. The acceleration traces are filtered between 1 and 10 Hz. The spectra in (b) and spectral ratio in (c) are smoothed by applying a mean smoothing algorithm with half width of 1 point.

HS $\beta_{FZ} = 1.5 \text{ km s}^{-1}$ and $\beta_{HS} = 3.2 \text{ km s}^{-1}$, and quality factors in the FZ and the HS $Q_{FZ} = 10$ and $Q_{HS} = 1000$. As mentioned, Ben-Zion *et al.* (2003) and Peng & Ben-Zion (2004) found that the FZ damaged layer in the study area is confined primarily to the top $\sim 3\text{--}4$ km. We thus put the shear dislocation source at the depth of 3 km inside the FZ and 90 m from the left-hand boundary near the right-hand FZ interface. Station VO is placed in the middle of the FZ at the free surface and station FP is placed ~ 400 m away from VO. We use the first 4 s of the calculated synthetic ground velocity records, transfer them into acceleration records and then compute the spectral ratio. An example is shown in Fig. 9 to illustrate the procedure.

To estimate the expected spectral changes associated with evolution of FZ properties, we compute spectral ratios from sets of synthetic seismograms generated by changing the seismic velocity in the FZ and keeping the other parameters the same as above. Fig. 10 shows spectral ratios obtained with five different values of β_{FZ} . As the β_{FZ} value is reduced from 2 to 1 km s^{-1} , the peak frequency decreases from 5.3 to 3.3 Hz and the peak spectral ratio increases from 4.9 to 7.3. These changes are consistent with the general patterns observed in Figs 5 and 6. We note that for a FZ width of 100 m, the peak frequency predicted from the basic relation $f = \beta_{FZ}/2W$ is 10 Hz for $\beta_{FZ} = 2 \text{ km s}^{-1}$, and 5 Hz for $\beta_{FZ} = 1 \text{ km s}^{-1}$. This value is higher than the simulation results because the synthetic calculations employ a very low quality factor $Q_{FZ} = 10$ inside the FZ. The associated high attenuation tends to shift the fundamental frequencies of FZ waves to lower values (e.g. Ben-Zion 1998). If we use the same quality factor of 1000 for both the FZ and HS, the obtained peak frequencies match the basic equation well.

To characterize better the likely changes of the FZ S -wave velocity, we perform synthetic simulations with β_{HS} values in the range from 0.5 to 3 km s^{-1} with increments of 0.01 km s^{-1} and search for

the values that best fit the observed peak frequency shifts (Fig. 6a). The best fitting velocities and the corresponding peak frequencies and peak spectral ratios are shown in Figs 11(a)–(c). The synthetic results indicate a reduction of the β_{FZ} value from $\sim 1.6 \text{ km s}^{-1}$ before the main shock to $\sim 0.97 \text{ km s}^{-1}$ immediately after the main shock (~ 40 per cent change) and near-complete recovery in ~ 1 d. We also perform a grid search of the FZ quality factor with the fixed β_{FZ} value of 1.5 km s^{-1} (Figs 11d–f). The results show that reducing the Q_{FZ} value can explain the observed peak frequency shift. However, in this case the peak spectral ratios decrease, which is in contrast to our observations. The simulations indicate that temporal changes of β_{FZ} values play a major part in causing the observed spectral changes. A more complete analysis will employ simultaneous changes of multiple parameters (e.g. β_{FZ} , Q_{FZ} and W values), but this is left for a future work.

5 COMPARISONS WITH PREVIOUS STUDIES

The Karadere segment of the NAF has been the focus of several detailed studies on spatio-temporal changes of FZ properties. Ben-Zion *et al.* (2003) performed a comprehensive analysis of seismic FZ trapped waves using the data set described in Section 2.1. They concluded that the trapped waves along the Karadere segment are generated by ~ 100 m wide FZ layers that extend primarily to $\sim 3\text{--}4$ km depth and are characterized by strong attenuation (Q values of $\sim 10\text{--}15$) and 30–50 per cent velocity reduction from that of the host rock. Systematic analyses of seismic anisotropy with fault-parallel cracks in the same area (Peng & Ben-Zion 2004, 2005) indicated that the trapping structures are surrounded by 1–2 km wide zones with lower damage, which also extend primarily to the top few kilometres of the crust. Peng & Ben-Zion (2006) and Karabulut & Bouchon (2007) observed clear temporal changes of seismic

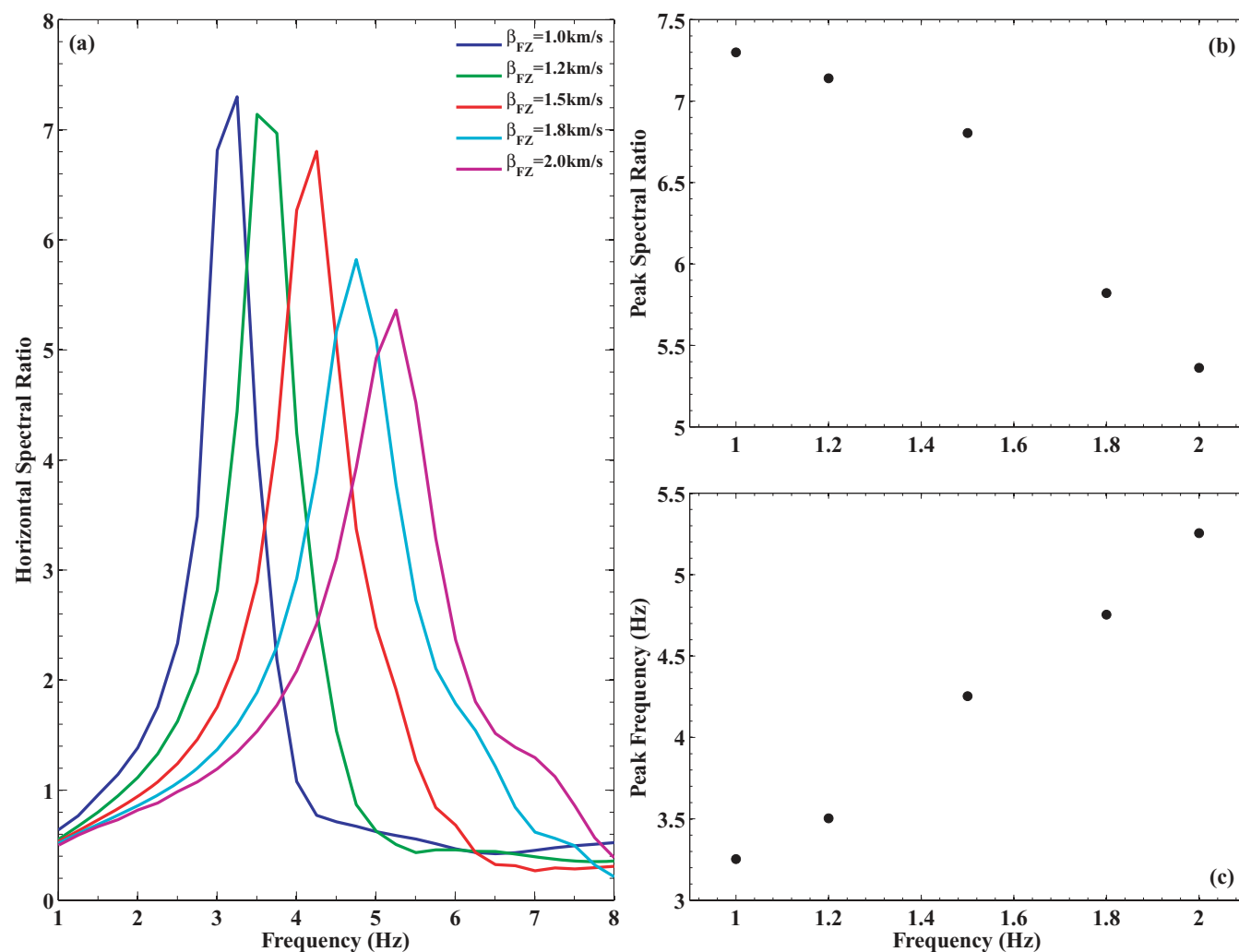


Figure 10. (a) Synthetic spectral ratios between stations VO and FP for five FZ S -wave velocities marked on the top right corner. (b) Peak spectral ratio and (c) peak frequencies plotted against FZ S -wave velocity for the traces shown in (a).

properties and non-linear wave propagation effects near the Karadere fault. The damaged FZ layers that produce trapped waves, seismic anisotropy, scattering, and non-linear wave propagation effects are all likely parts of a hierarchical flower structure that resides primarily above the seismically-active portion of the crust. The anomalous wave propagation effects of the shallow damaged FZ layers may be referred to collectively as FZ-related site effects (Ben-Zion *et al.* 2003).

Peng & Ben-Zion (2006) used a moving-window waveform cross-correlation technique to monitor the temporal changes of seismic velocities after the Düzce main shock, using weak motion generated by repeating earthquakes. They found clear step-like co-main shock changes followed by logarithmic recovery over a timescale of at least 3 months in direct S and early S coda waves (Fig. 12a). The spectral ratio analysis of the strong ground motion in this study indicates ~ 20 – 40 per cent reduction of the peak frequency and recovery with timescale of 1 d. The spectral ratio analysis of weak motion in this study shows a mild recovery over the 3 months duration of the data within large scatter. Assuming that the observed temporal changes are accumulated in the top ~ 3 km of the crust (Ben-Zion *et al.* 2003), the coseismic change of seismic velocities extrapolated to the main shock time is on the order of a few per cent.

However, if we assume that the thickness of the layer responsible for the temporal changes is only ~ 300 m (e.g. Rubinstein & Beroza 2005), the inferred coseismic velocity change at the FZ station VO is about 17 per cent (Fig. 12b). This value is much closer to the ~ 45 per cent changes observed by Karabulut & Bouchon (2007) and in this study. Further decreasing the layer thickness to smaller values like 100 m would result in a better match of the coseismic changes. As summarized in Fig. 12, our spectral ratio results based on the strong motion data indicate a recovery timescale of ~ 1 d, which is much shorter than the ~ 3 month timescale of Peng & Ben-Zion (2006) but significantly longer than the near-instantaneous recovery inferred by Karabulut & Bouchon (2007).

One possible explanation for the different results is the differences in the timescale of the usable data. The coseismic change and the apparent recovery within 1 d observed in this study are obtained from on-scale strong motion recordings during and immediately after the main shock (Figs 5–7). As noted in Section 3, most of the weak motion recordings are saturated in this time period, thus preventing similar analysis based on repeating earthquakes (e.g. Peng & Ben-Zion 2006). Some waveforms may be clipped or buried inside seismograms of other events immediately after the main shock, and many earthquakes (including repeating events) are not detected

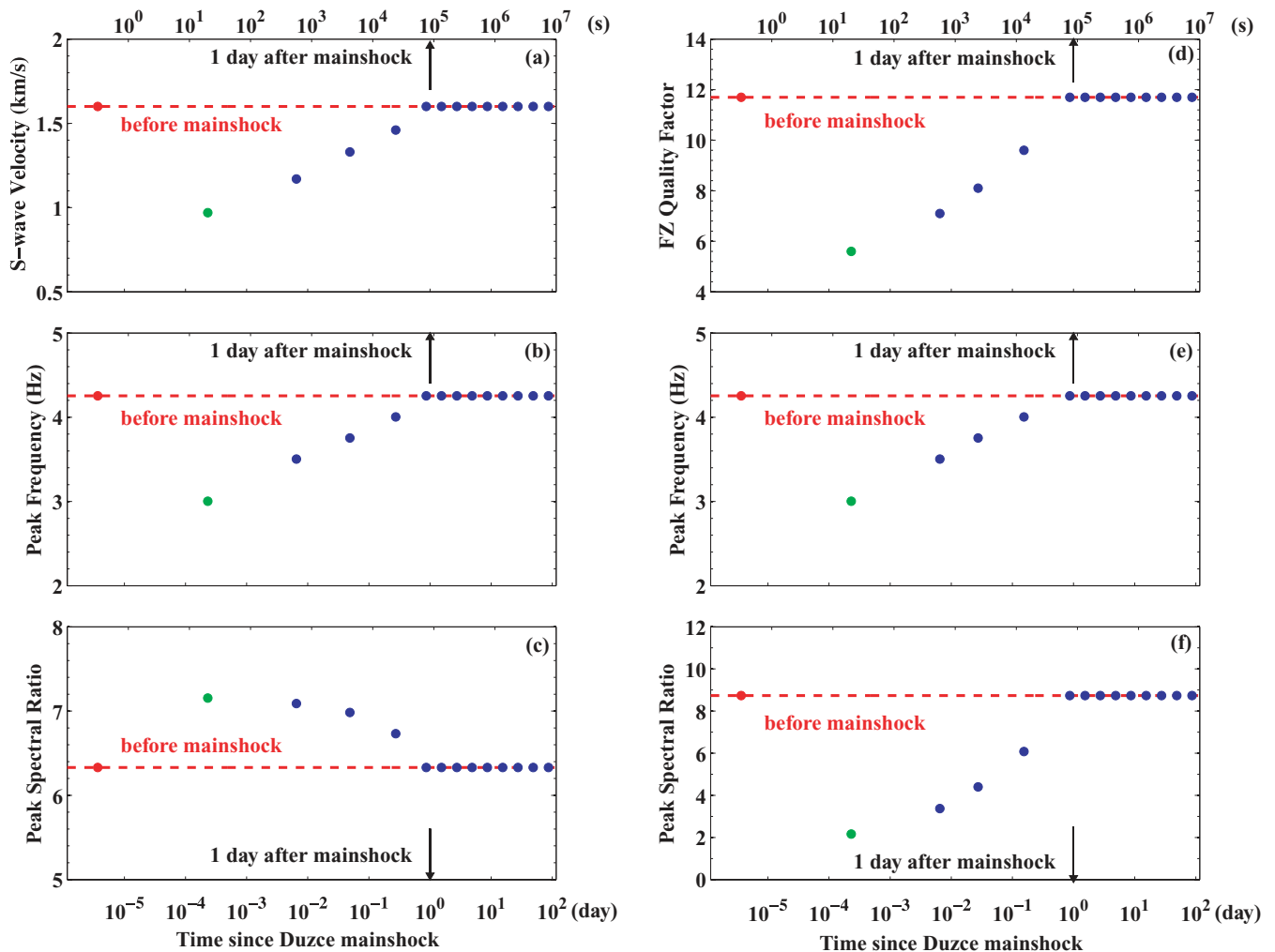


Figure 11. (a) Best-fitting S -wave velocities from waveform simulation inside the FZ before (red), during (green) and after (blue) the main shock to the observed frequency shifts in Fig. 6(a). The red dashed line indicates the pre-main shock value. The vertical black arrow marks the time of 1 d after the main shock. Values shown on the top and bottom of the figure indicate lapse times after the main shock in seconds and in days, respectively. (b) Synthetic peak frequencies and (c) synthetic peak spectral ratios by varying the FZ S -wave velocity, with the same symbols and notations as (a). (d) Best-fitting quality factor from waveform simulation. (e) Synthetic peak frequencies and (f) synthetic peak spectral ratios by varying FZ Q value.

in the standard earthquake catalogues (e.g. Peng *et al.* 2006, 2007; Enescu *et al.* 2007). A systematic search for repeating earthquakes in the early aftershock period (e.g. Peng & Zhao 2008) could provide useful information on the coseismic changes in material properties of the shallow crust and how they evolve within the initial minutes to hours after the main shock.

Another basic explanation for the differences of results is the use of different analysis techniques. In this study, we employ station FP as the reference site for the spectral ratio calculations. However, as shown by Peng & Ben-Zion (2006) and Fig. 12(a), changes of seismic velocities are observed at both stations VO and FP during the Düzce main shock, although the degree of change at FP is smaller than that at VO. It is therefore clear that calculations based on the spectral ratios between these two stations give lower bound values for both the amplitude of the co-main shock change at station VO and the timescale of recovery. The spectral ratios of the strong motion records provide relatively high-resolution results on the very early large temporal changes of FZ properties following the Düzce main shock. The lower-amplitude longer-duration variations that occur at both stations are generally beyond the sensitivity of the

spectral ratio analysis, as evident by the relatively constant values and large error bars for both the strong and weak motion data. Such subtle changes could be measured better by the repeating earthquakes analysis (e.g. Peng & Ben-Zion 2006).

The difference in the timescale of recovery between our results and those from Karabulut & Bouchon (2007) probably also stems from differences in the data sets and analysis procedures. In this study, we analysed both weak and strong motion recordings from several days before to 72 d after the Düzce main shock. In addition, the distance between the station pair employed in this study is ~ 400 m, smaller than the 1.5 km distance for the station pair used by Karabulut & Bouchon (2007). Since we analysed a larger data set having smaller path effects, we are probably able to observe finer details of the very-early strong co-main shock changes and the more subtle longer-duration recovery process.

6 DISCUSSION

Many factors could contribute to the temporal changes of seismic spectra observed in this study. These include apparent changes

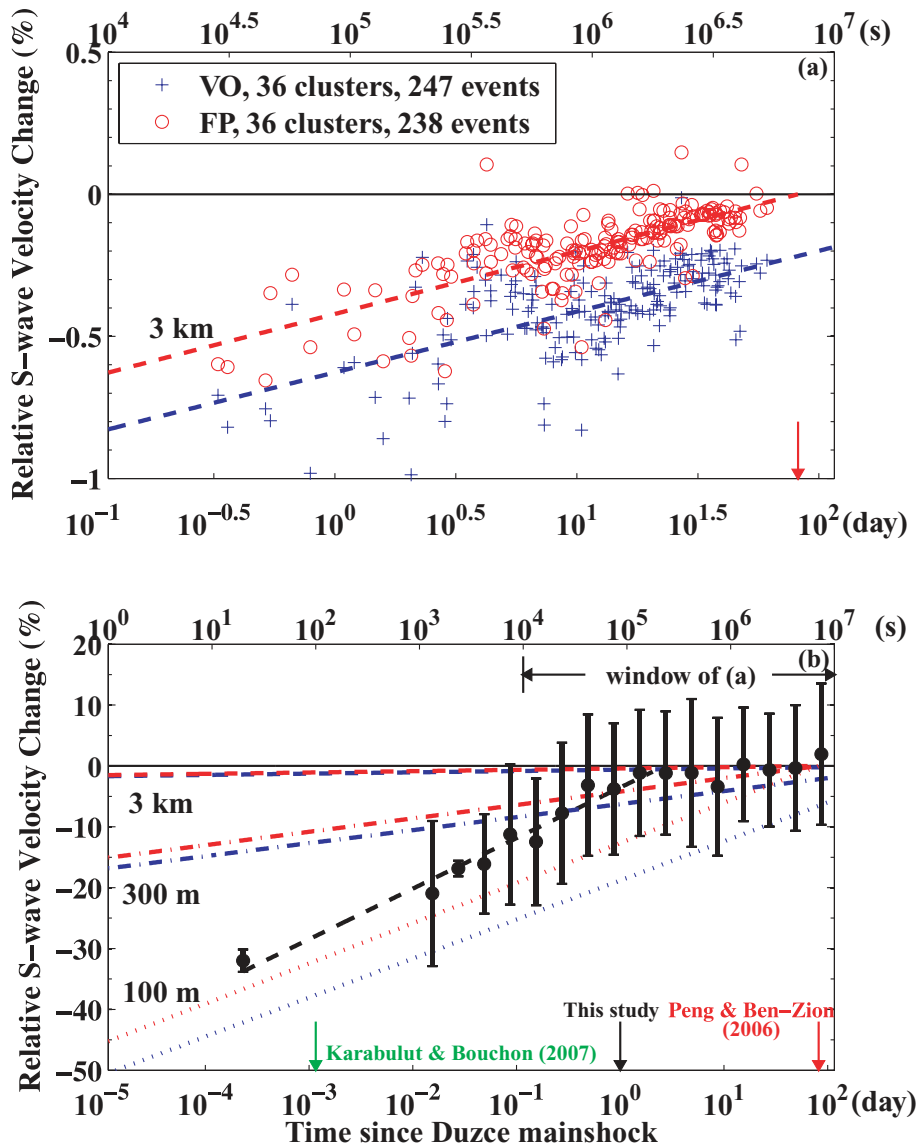


Figure 12. (a) Relative *S*-wave velocity changes inferred from time delays for early *S*-coda waves by Peng & Ben-Zion (2006). The blue crosses and red circles show measurements for stations VO and FP, respectively. The horizontal black solid line indicates the pre-main shock level of 0 per cent. The blue and red dashed lines are least-squares fits to the data, and the red arrow indicates the recovery time of at least 3 months. Values shown at the top and bottom of the figure indicate lapse times after the Düzce main shock in seconds and in days, respectively. (b) Relative *S*-wave velocity changes measured from the averaged peak frequencies for the coda-window based analysis. Vertical solid bar centred at each data point shows the standard deviation. The black dashed line shows the least-squares fit to the data observed in this study. The blue (VO) and red (FP) dashed lines, dash-dot lines and dotted lines show the least-squares fits to the data shown in (a) assuming that temporal changes occur in the top 3 km, 300 m and 100 m, respectively. The green, black and red arrows mark the time scale of recovery of ~ 100 s inferred by Karabulut & Bouchon (2007), ~ 1 d in this study and at least 3 months by Peng & Ben-Zion (2006), respectively.

produced by varying radiation from sources at different locations, and physical changes occurring in shallow sediments and within the damaged FZ rocks. Because the two employed stations are very close to each other (~ 400 m) compared with the distances between the earthquakes sources and stations (typically more than 10 km), apparent changes from variable source locations are unlikely to be the reason for the observed changes. The presence of hard rock outcrops near the two stations VO and FP (Herece & Akay 2003) and the location of station VO within the FZ, reduce the likelihood that the results are dominated by shallow sediments, although such changes can contribute to the observations.

Temporal changes of seismic properties within the damaged FZ rocks that are initiated by the strong ground motion of the Düzce

main shock are likely to be the main origin of the observed variations of the spectral ratios and peak frequencies. As suggested by the synthetic waveform simulations, the abrupt co-main shock changes are likely associated with reduction of seismic velocity in the FZ layer and to a lesser extent probably also reduction of the FZ attenuation coefficient. Such changes involve physically increasing crack and void densities in the shallow FZ structure, which can be generated by opening and growth of cracks inside the FZ and possibly also reduced packing of the near-surface granular material. During the post-main shock period, the normal stress produces reversed processes associated with decreasing density of crack surfaces and increasing sediment packing. These healing processes produce logarithmic recovery of properties that approach asymptotically the

pre-main shock levels. The discussed effects are observed in laboratory experiments with granular material and rocks (e.g. Dieterich & Kilgore 1996; Scholz 2002; Johnson & Jia 2005) and may be simulated using damage rheology models (e.g. Hamiel *et al.* 2004; Finzi *et al.* 2008; Lyakhovskiy & Ben-Zion 2008).

The opening and growth of cracks in the damaged FZ material during strong ground motion is expected to increase the contrast of the seismic velocity across the FZ. This can increase the amplification of ground motion within the FZ, although part of the seismic energy could be consumed in the crack opening and growth processes and the amplification may be reduced partially by increasing attenuation. It is important to try to separate effects associated with reduced seismic velocities and increasing attenuation. However, detailed investigation of temporal changes in attenuation of the FZ material requires nearly identical microseismic sources (e.g. Bokelmann & Harjes 2000; Chun *et al.* 2004) to preclude source, path and other variations, which is beyond the scope of this study.

It is not clear what parameters control the timescale of recovery. Previous studies suggested that diffusion of fluids may play an important role in the coseismic reduction and postseismic logarithmic recovery (e.g. Schaff & Beroza 2004; Sawazaki *et al.* 2006). However, logarithmic recovery is also expected due to generic enlargement of the real contact area of crack surfaces and grain contacts under normal stress (e.g. Marone 1998; Johnson & Sutin 2005). Although there is no direct evidence for the presence of fluids in our study area, many studies have observed widespread increase of water flow after several major earthquakes (e.g. Rojstaczer *et al.* 1995; Brodsky *et al.* 2003; Wang *et al.* 2004; Manga & Wang 2007). They proposed that increasing permeability in the near-surface layers due to strong shaking from the main shock is the main cause of increased fluid flow. Sawazaki *et al.* (2006) found a 30–70 per cent reduction of the peak frequencies in the coda-window-based spectral ratios using data recorded by vertical borehole arrays during the 2000 Western Tottori and 2003 Tokachi-Oki Earthquake sequences in Japan. The coseismic reduction is followed by a logarithmic recovery to pre-main shock value with timescales ranging from a few tens of minutes at a soft sandy gravel site to a few years at solid and weathered hard rock sites. If fluids play an important role in the process, the observed timescale could be mainly controlled by the permeability at each site, which is related to the specific site conditions, and would increase with the amplitude of seismic waves (Elkhoury *et al.* 2006). Additional field and laboratory studies are needed to clarify the precise processes controlling the coseismic changes and timescale of the recovery process.

Our observations and the results of Karabulut & Bouchon (2007) of large coseismic reduction of seismic velocities at FZ sites support the notion (e.g. Beresnev & Wen 1996; Field *et al.* 1997) that non-linearity is widespread in the shallow crust during strong ground motion of moderate to large earthquakes. The analysis done in this study provides a bridge between the large-amplitude near-instantaneous changes inferred by Karabulut & Bouchon (2007) and the lower-amplitude longer-duration variations inferred by Peng & Ben-Zion (2006). The changes observed by the spectral ratio analysis provide a refinement for the beginning of the longer more gradual process observed by Peng & Ben-Zion (2006) and other related works based on waveform analysis of repeating earthquakes (e.g. Rubinstein & Beroza 2004a, b, 2005; Rubinstein *et al.* 2007).

ACKNOWLEDGMENTS

We thank Tim Long, Andy Newman and Dominic Assimaki for useful comments on an early version of the manuscript. The manuscript

benefited from valuable comments by Haruo Sato, an anonymous referee and editor John Beavan. The study was supported by the National Science Foundation (grant EAR-0710959) and the Southern California Earthquake Center (NSF Cooperative Agreement EAR-0529922 and USGS Cooperative Agreement 07HQAG0008). The SCEC contribution number for this paper is 1242.

REFERENCES

- Aki, K., 1969. Analysis of the seismic coda of local earthquakes as scattered waves, *J. geophys. Res.*, **74**, 615–631.
- Aki, K. & Chouet, B., 1975. Origin of coda waves: source, attenuation, and scattering effects, *J. geophys. Res.*, **80**, 3322–3342.
- Aster, R.C. & Shearer, P.M., 1991. High-frequency borehole seismograms recorded in the San Jacinto Fault Zone, southern California, Part 2: attenuation and site effects, *Bull. seism. Soc. Am.*, **81**, 1081–1100.
- Ben-Zion, Y., 1998. Properties of seismic fault zone waves and their utility for imaging low velocity structures, *J. geophys. Res.*, **103**, 12567–12585.
- Ben-Zion, Y. & Aki, K., 1990. Seismic radiation from an SH line source in a laterally heterogeneous planar fault zone, *Bull. seism. Soc. Am.*, **70**, 971–994.
- Ben-Zion, Y. & Sammis, C.G., 2003. Characterization of fault zones, *Pure appl. Geophys.*, **160**, 677–715.
- Ben-Zion, Y. & Shi, Z., 2005. Dynamic rupture on a material interface with spontaneous generation of plastic strain in the bulk, *Earth planet. Sci. Lett.*, **236**, 486–496.
- Ben-Zion, Y. *et al.*, 2003. A shallow fault-zone structure illuminated by trapped waves in the Karadere-Düzce branch of the North Anatolian Fault, western Turkey, *Geophys. J. Int.*, **152**, 699–717.
- Beresnev, I.A. & Wen, K.L., 1996. Review nonlinear soil response—a reality? *Bull. seism. Soc. Am.*, **86**, 1964–1978.
- Bokelmann, G.H.R. & Harjes, H.P., 2000. Evidence for temporal variation of seismic velocity within the upper continental crust, *J. geophys. Res.*, **105**, 23 879–23 894.
- Brodsky, E.E., Roeloffs, E., Woodcock, D., Gall, I. & Manga M., 2003. A mechanism for sustained ground water pressure changes induced by distant earthquakes, *J. geophys. Res.*, **108**, doi:10.1029/2002JB002321.
- Castro, R.R., Mucciarelli, M., Pacor, F. & Petrongaro, C., 1997. S-wave site-response estimates using horizontal-to-vertical spectral ratio, *Bull. seism. Soc. Am.*, **87**(1), 256–260.
- Chun, K.-Y., Henderson, G.A. & Liu J., 2004. Temporal changes in P wave attenuation in the Loma Prieta rupture zone, *J. geophys. Res.*, **109**, B02317, doi:10.1029/2003JB002498.
- Dieterich, J.H. & Kilgore, B.D., 1996. Imaging surface contacts: power law contact distributions and contact stresses in quartz, calcite, glass, and acrylic plastic, *Tectonophysics*, **256**, 219–239.
- Elkhoury, J.E., Brodsky, E.E. & Agnew, D.C., 2006. Seismic waves increase permeability, *Nature*, **441**, 1135–1138.
- Enescu, B., Mori, J. & Miyazawa, M., 2007. Quantifying early aftershock activity of the 2004 mid-Niigata Prefecture earthquake (Mw6.6), *J. geophys. Res.*, **112**, B04310, doi:10.1029/2006JB004629.
- Field, E.H., Johnson, P.A., Beresnev, I.A., & Zeng, Y., 1997. Nonlinear ground-motion amplification by sediments during the 1994 Northridge earthquake, *Nature*, **390**, 599–602.
- Finzi, Y., Hearn, E.H., Ben-Zion, Y. & Lyakhovskiy V., 2008. Structural properties and deformation patterns of evolving strike-slip faults: numerical simulations incorporating damage rheology, *Pure appl. Geophys.*, in press.
- Goldstein, P., Dodge, D., Firpo, M. & Minner, L., 2003. SAC2000: signal processing and analysis tools for seismologists and engineers (Chapter 85.5), in *The IASPEI International Handbook of Earthquake and Engineering Seismology Part B*, eds Lee, W.H.K., Kanamori, H., Jennings, P.C. & Kisslinger C., Academic Press, London.
- Hamiel, Y., Liu, Y., Lyakhovskiy, V., Ben-Zion, Y. & Lockner, D., 2004. A viscoelastic damage model with applications to stable and unstable fracturing, *Geophys. J. Int.*, **159**, 1155–1165, doi: 10.1111/j.1365-246X.2004.02452.x.

- Herece, E. & Akay, E., 2003. 1:100,000 geological maps of the North Anatolian Fault, Appendix 3 and 4, Gen. Dir. of Miner. Res. and Explor., Ankara.
- Johnson, P.A. & Jia, X., 2005. Nonlinear dynamics, granular media and dynamic earthquake triggering, *Nature*, **473**, 871–874.
- Johnson, P.A. & Sutin, A., 2005. Slow dynamics and anomalous nonlinear fast dynamics in diverse solids, *J. acoust. Soc. Am.*, **117**, 124–130.
- Karabulut, H. & Bouchon, M., 2007. Spatial variability and non-linearity of strong ground motion near a fault, *Geophys. J. Int.*, **170**, 262–274.
- Li, Y.G., Vidale, J.E., Aki, K., Xu, F. & Burdette, T., 1998. Evidence of shallow fault zone strengthening after the 1992 M7.5 Landers, California, earthquake, *Science*, **279**, 217–219.
- Li, Y.G., Chen, P., Cochran, E.S., Vidale, J.E. & Burdette, T., 2006. Seismic evidence for rock damage and healing on the San Andreas fault associated with the 2004 M 6.0 Parkfield earthquake, *Bull. seism. Soc. Am.*, **96**, 349–363.
- Lyakhovskiy, V. & Ben-Zion, Y., 2008. Scaling relations of earthquakes, aseismic deformation and evolving fault structures in a damage rheology model, *Geophys. J. Int.*, **172**, 651–662, doi:10.1111/j.1365-246X.2007.03652.x.
- Lyakhovskiy, V., Ben-Zion, Y. & Agnon, A., 1997. Distributed damage, faulting and friction, *J. geophys. Res.*, **102**, 27 635–27 649.
- Manga, M. & Wang C.-Y., 2007. Earthquake hydrology, in *Treatise on Geophysics*, Vol. 4, pp. 293–320, ed. Schubert G, Elsevier Science, Amsterdam.
- Marone, C., 1998. Laboratory-derived friction laws and their application to seismic faulting, *An. Rev. Earth planet. Sci.*, **26**, 643–649.
- Mavko, G. T., Mukherji, T. & Dvorkin, J., 1998. *The Rock Physics Handbook-Tools for Seismic Analysis in Porous Media*, Cambridge University Press, New York.
- Mayedá, K., Malagnini, L. & Walter, W.R., 2007. A new spectral ratio method using narrow band coda envelopes: evidence for non-self-similarity in the Hector Mine sequence, *Geophys. Res. Lett.*, **34**, L11303, doi: 10.1029/2007GL030041.
- Pavlenko, O.V. & Irikura, K., 2003. Estimation of nonlinear time-dependent soil behavior in strong ground motion based on vertical array data, *Pure appl. Geophys.*, **160**, 2365–2379.
- Peng, Z. & Ben-Zion, Y., 2004. Systematic analysis of crustal anisotropy along the Karadere-Düzce branch of the north Anatolian fault, *Geophys. J. Int.*, **159**, 253–274, doi:10.1111/j.1365-246X.2004.02379.x.
- Peng, Z. & Ben-Zion, Y., 2005. Spatiotemporal variations of crustal anisotropy from similar events in aftershocks of the 1999 M7.4 İzmit and M7.1 Düzce, Turkey, earthquake sequences, *Geophys. J. Int.*, **160**, 1027–1043.
- Peng, Z. & Ben-Zion, Y., 2006. Temporal changes of shallow seismic velocity around the Karadere-Düzce branch of the North Anatolian Fault and strong ground motion, *Pure appl. Geophys.*, **163**, 567–600, doi:10.1007/s00024-005-0034-6.
- Peng, Z. & Zhao, P., 2008. Early aftershocks of the 2004 Parkfield earthquake detected by a matched filter technique, *Seis. Res. Lett.*, **79**(2), 303.
- Peng, Z., Vidale, J. E. & Houston, H., 2006. Anomalous early aftershock decay rates of the 2004 M6 Parkfield earthquake, *Geophys. Res. Lett.*, **33**, L17307, doi:10.1029/2006GL026744.
- Peng, Z., Vidale, J. E., Ishii, M. & Helmstetter, A., 2007. Seismicity rate immediately before and after main shock rupture from high-frequency waveforms in Japan, *J. geophys. Res.*, **112**, B03306, doi:10.1029/2006JB004386.
- Phillips, W.S. & Aki, K., 1986. Site amplification of coda waves from local earthquakes in central California, *Bull. seism. Soc. Am.*, **76**, 627–648.
- Relinger, R.E. et al., 1997. Global Positioning System measurements of the present day crustal movements in the Arabia-Africa-Eurasia plate collision zone, *J. geophys. Res.*, **102**, 9983–9999.
- Rice, J.R., Sammis, C.G. & Parsons, R., 2005. Off-fault secondary failure induced by a dynamic slip-pulse, *Bull. seism. Soc. Am.*, **95**(1), 109–134, doi:10.1785/0120030166.
- Rojstaczer, S.A., Wolf, S.C. & Michel, R.L., 1995. Permeability enhancement in the shallow crust as a cause of earthquake-induced hydrological changes, *Nature*, **373**, 237–239.
- Rubinstein, J.L. & Beroza, G.C., 2004a. Evidence for widespread nonlinear strong ground motion in the Mw 6.9 Loma Prieta Earthquake, *Bull. seism. Soc. Am.*, **94**, 1595–1608.
- Rubinstein, J.L. & Beroza, G.C., 2004b. Nonlinear strong ground motion in the M15.4 Chittenden earthquake: evidence that pre-existing damage increases susceptibility to further damage, *Geophys. Res. Lett.*, **31**, L23614, doi:10.1029/2004GL021357.
- Rubinstein, J.L. & Beroza, G.C., 2005. Depth constraints on nonlinear strong ground motion, *Geophys. Res. Lett.*, **32**, L14313, doi:10.1029/2005GL023189.
- Rubinstein, J.L., Uchida, N. & Beroza, G.C., 2007. Seismic velocity reductions caused by the 2003 Tokachi-Oki earthquake, *J. geophys. Res.*, **112**, B05315, doi:10.1029/2006JB004440.
- Sawazaki, K., Sato, H., Nakahara, H. & Nishimura, T., 2006. Temporal change in site response caused by earthquake strong motion as revealed from coda spectral ratio measurement, *Geophys. Res. Lett.*, **33**, L21303, doi:10.1029/2006GL027938.
- Sawazaki K., Sato, H., Nakahara, H., & Nishimura, T., 2008. Drop and recovery process of seismic velocity in the shallow ground caused by strong ground motion shock as revealed from coda deconvolution analysis, *Bull. seism. Soc. Am.*, in press.
- Schaff, D.P. & Beroza, G.C., 2004. Coseismic and postseismic velocity changes measured by repeating earthquakes, *J. geophys. Res.*, **109**, B10302, doi:10.1029/2004JB003011.
- Scholz, C.H., 2002. *The Mechanics of Earthquakes and Faulting*, 2nd edn, Cambridge University Press, New York, 471 pp.
- Seeber, L., Armbruster, J.G., Ozer, N., Aktar, M., Baris, S., Okaya, D., Ben-Zion, Y. & Field, E., 2000. The 1999 earthquake sequence along the North Anatolia transform at the juncture between the two main ruptures, in *The 1999 İzmit and Düzce Earthquakes: Preliminary Results*, pp. 209–223, eds Barka, A., Kozaci, O., Akyuz, S. & Altunel, E., Istanbul Technical University, Turkey.
- Vidale, J.E. & Li, Y.G., 2003. Damage to the shallow Landers fault from the nearby Hector Mine earthquake, *Nature*, **421**, 524–526.
- Wang, C.Y., Wang, C.-H. & Manga, M., 2004. Coseismic release of water from mountains: evidence from the 1999 (Mw = 7.5) Chi-Chi, Taiwan, earthquake, *Geology*, **32**, 769–772.
- Yang, W., Ben-Zion, Y. & Peng, Z., 2007. Correcting clipped seismic waveform by using waveforms of similar events, *Seism. Res. Lett.*, **78**, 249.